Journal of Aerosol Science 161 (2022) 105946

Contents lists available at ScienceDirect

Journal of Aerosol Science

journal homepage: www.elsevier.com/locate/jaerosci

Particle deposition characteristics in the formation of Hard Grey Scale (HGS) on cold surfaces exposed to aluminium production off-gas

Daniel Perez Clos [a,*], Hannes Zedel [a], Sverre Gullikstad Johnsen [a,b], Petter Nekså [c], Ragnhild E. Aune [a]

[a] Department of Materials Science and Engineering, Norwegian University of Science and Technology (NTNU), Trondheim, Norway
[b] SINTEF Industry, Trondheim, Norway
[c] SINTEF Energy Research, Trondheim, Norway

ARTICLE INFO

Keywords:
Aluminium industry
Fouling
Hard grey scale
Particle size distribution
Image analysis

ABSTRACT

Hard Grey Scale (HGS) is a hard and strongly adhering fouling material that forms on solid surfaces impinged by the off-gas generated in the pot cells of aluminium production plants. Different theories on HGS formation mechanisms have been suggested, involving particle re-crystallization or formation of a binder phase between the deposited particles. However, no conclusive proofs have yet been presented. This study focuses on statistical quantification of HGS growth rates and particle deposition characteristics from analysis of fouling experiments in a primary aluminium production plant. The experiments were performed with a cylindrical cold-finger inserted in a duct upstream of the Gas Treatment Center (GTC) with durations ranging from a few hours to several months. Detailed characterization of cold-finger deposits and off-gas particle size distributions was performed using image analysis (IA) and a Particle Diffraction Sizer (PDS) to investigate particle capture efficiencies on both sides of the cold-finger. In addition, an old HGS sample from a secondary alumina transport pipe, with different appearance than cold-finger HGS, was analyzed. Results show that HGS particles have a log-normal size distribution centered at 1.2 μm with 35% of the particles below 1 μm. A similar granular structure and size distribution was found for the HGS sample from the secondary alumina transport pipe, suggesting that a similar formation mechanism exists for the two types of HGS. Particle capture efficiency results for cold-finger HGS at low Stokes numbers are in good agreement with numerical studies considering inertial impaction efficiencies. At larger Stokes numbers, i.e. larger particle sizes, rebounding and re-entrainment effects result in lower capture efficiencies than those predicted by the impaction models. The present results suggest that HGS formation is due to inertial deposition of small particles, with the submicron-sized fraction generating a closely packed structure responsible for the HGS bulk properties.

1. Introduction

Fouling is defined as the unwanted accumulation of solid deposits on solid surfaces. Fouling occurs in many varieties in a wide

* Corresponding author.
E-mail address: danipclos@gmail.com (D. Perez Clos).

https://doi.org/10.1016/j.jaerosci.2021.105946
Received 25 June 2021; Received in revised form 13 December 2021; Accepted 24 December 2021
Available online 28 December 2021

range of industrial applications. Scaling, which is defined as precipitation fouling, occurs typically due to supersaturation of solutions. E.g., the precipitation of limescale in aqueous systems, results in hard and compact deposits strongly adhering to solid surfaces. Particulate fouling is formed by the deposition of suspended particles from a fluid to a solid surface by mechanisms such as sedimentation, inertial impaction, Brownian diffusion, and thermophoresis, among others (Boerlage, 2001; Bott, 1995).

In the aluminium industry, Hard Grey Scale (HGS) is a specific notation (Dando & Lindsay, 2008) used about the type of particulate fouling that produces layers of deposited material with similar bulk properties to scaling processes in terms of hardness and surface adhesion. The somewhat misleading term "scale" was probably given due to the similarities with precipitated scale observed in other industrial processes.

HGS is reported to form in areas where the particle-laden gas impinges a surface, where it can grow with large aspect ratios. This is especially problematic in dry scrubber components such as dribble plate orifices, diffuser plates and filter bags, as well as in pipe bends (Dando & Lindsay, 2008).

In dry scrubbers, Smelter Grade Alumina (SGA) or "primary" alumina is used to absorb Hydrogen Fluoride (HF) from the off-gas. Intimate contact between the two streams is achieved by means of fluidized beds or alumina injection systems. The resulting reacted alumina or "secondary" alumina is then transported by pneumatic conveyors to the electrolysis cells together with the particles from the off-gas captured in the filter bags, which are periodically released to the secondary alumina stream (Lindsay & Dando, 2009).

A different type of HGS forms in the secondary alumina transport pipes which has a brighter grey color than that produced in the cold-finger. The fact that primary alumina transport pipes do not suffer from HGS formation (Lindsay & Dando, 2009) clearly indicates that a key component from the off-gas must trigger HGS growth in secondary alumina streams.

HGS formation in the aluminium production industry has been a problem for decades causing periodic shut-downs and expensive cleaning procedures (Bott, 1995). However, only few studies that specifically address HGS formation have been published, resulting in the suggestion of different formation mechanisms based on particles recrystallization ((Dando & Lindsay, 2008), (Gaertner et al., 2014)), presence of a binder phase (Bock Haugland et al., 2019) and mechanical deposition of highly adhesive submicron particles (Clos et al., 2019).

To further elucidate the HGS particle deposition characteristics, results from different fouling experiments are presented in this study. The experiments were conducted in an aluminium production plant based on the Hall–Héroult process. HGS samples were

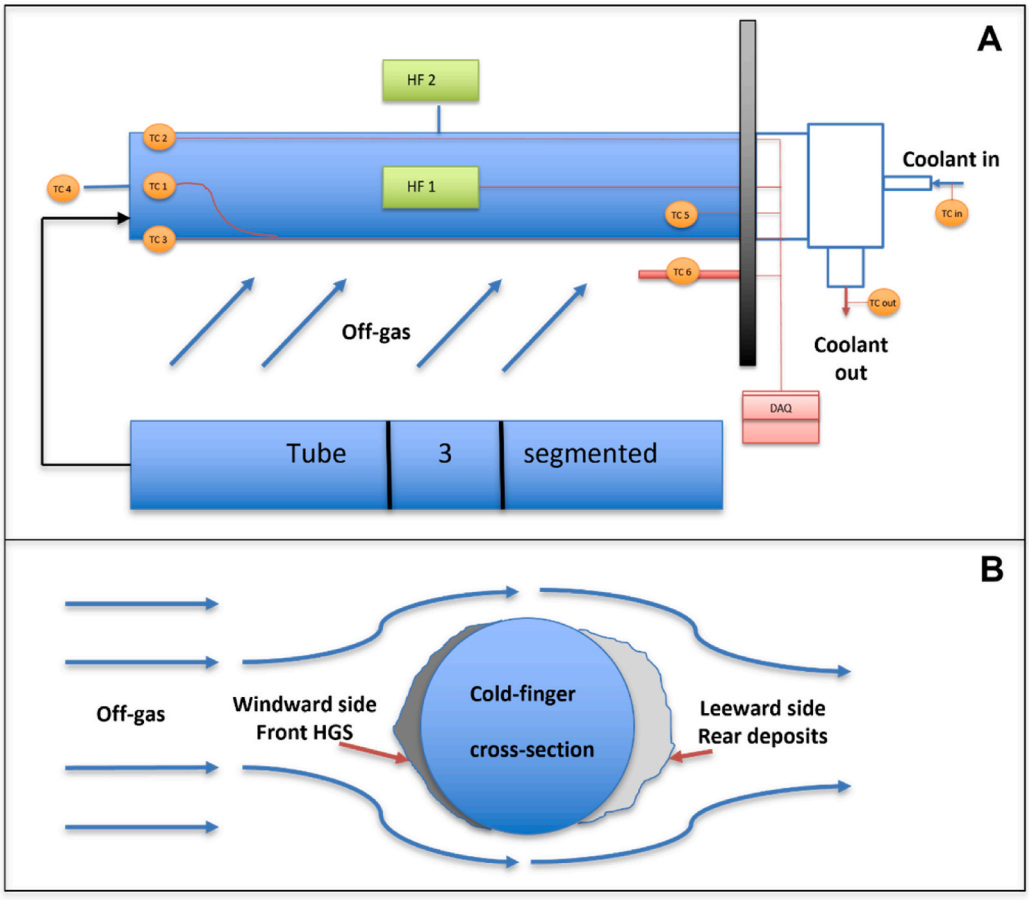

Fig. 1. Diagram showing the cold-finger cross section and the deposits location.

collected in a cylindrical fouling probe or "cold-finger" inserted in crossflow to a duct transporting the off-gas generated by the electrolysis cells to the gas treatment center.

Particle size distribution of deposits and off-gas dust samples were analyzed by Image Analysis (IA) on electron images and Particle Diffraction Sizer (PDS) technique to investigate deposits growth rates and particle capture efficiencies on the surface of the probe. In addition, an HGS sample from a secondary alumina transport pipe produced in a different study by Haugland et al. (Bock Haugland et al., 2019) was analyzed by IA and compared with HGS from cold-finger experiments.

2. Methodology

2.1. Cold-finger experiments

A half-meter long cylindrical cold-finger was used in the present fouling experiments. The probe has a 3 tube-in-tube configuration with an outer diameter of 35 mm and a coolant flowing in the inner sections. Thermocouples (TC) and heat flux sensors (HF) placed on the surface of the center tube, allow for surface temperature and heat flux monitoring (see Fig. 1A). The outermost sleeve, which was replaced after each experiment, covers and protects the sensors and is the substrate on which particle deposition occurs. Temperatures in the off-gas duct oscillated between 90 and 120 °C from winter to summer depending on weather conditions.

Before starting the experiments, the coolant flow (pressurized air) was started, and the temperature and heat-flux logging system was initialized. The cold-finger was then introduced to the off-gas duct through a flange opening upstream of the GTC. The probe was oriented in cross-flow with the off-gas. The nature and appearance of the deposits varied significantly around the cold-finger circumference as depicted in Fig. 1B. HGS formed on the front side of the cold-finger (windward side) while loosely attached, dusty particles accumulated on the rear side (leeward side), which from here and onwards will be referred to as "rear deposits".

To investigate the deposition rate as a function of time, a series of experiments with different durations were conducted. At the end of each experiment, the cold-finger was extracted from the flange and allowed to cool down, by maintaining the coolant flow for about 2 min before removing the outer tube with the deposits.

The outer tube was segmented axially into three pieces before the experiments with fringes that allowed easy coupling and decoupling of the pieces.

The center piece was then carefully separated to avoid loss of the loosely attached rear deposits. Thereafter, the piece was introduced in a specially designed metal box, cast in epoxy, sliced and polished in order to analyse the pipe/deposits cross section by electron microscopy and IA. Samples from the front (front HGS) and rear (rear deposits) sides were scratched off from the two remaining pieces and collected in separate glass containers for analysis by PDS. No indication that the morphology of the deposits varied along the length of the cold-finger was observed.

Data from experiments of different durations ranging from three hours to eight months are presented in this study. Three of these experiments were performed without cooling flow in order to investigate thermophoretic effects.

2.2. Off-gas particle analysis

Iso-kinetic sampling of the off-gas particles with particle collection on filters were performed on several occasions in a flange opening adjacent to the cold-finger. The collected dust was analyzed both by PDS and suspended in epoxy and polished for electron microscopy analysis.

2.3. Deposits density estimation

The mass density of HGS (ρ_s) was measured by submerging weighted pieces of HGS in a graduated cylinder with ethanol to measure the corresponding volume. The mass density of the rear deposits (ρ_r) was estimated by weighting a container of known volume filled with deposits scratched from the cold-finger after an experiment.

2.4. Particle size distribution estimation

Two different methods (IA and PDS) were employed to establish particle size distributions of the different samples collected in the experiments.

2.4.1. Electron microscope image analysis (IA)

A JEOL JXA-8500F Electron Probe Micro Analyzer (EPMA) was used to obtain Secondary Electron (SE) and Back-Scattered Electron (BSE) images of the deposits and off-gas samples. A 15 kV acceleration voltage was used with 20 nA beam current. Images were used to estimate deposits layer thicknesses (tube-deposit cross-section) and to determine particle size distributions using IA.

Front HGS and rear deposits samples from five different experiments as well as five off-gas samples, were analyzed as follows to calculate average particle size distribution values with statistical significance.

Each sample was analyzed by taking SE and BSE electron image pairs of several randomly zoomed-in areas. The difference in contrast between image pairs was used to improve the differentiation between individual particles.

For the quantitative assessment of particle size distributions, a deterministic grey-scale thresholding method was adapted. This method was previously used to identify particle inclusions in aluminium melt SEM images and thus to quantify filtration efficiency

(Zedel et al., 2019).

The IA algorithm applies a gaussian filter and isolates grey scale ranges for binarization of the relevant phases. Post-processing involves basic artefact removal, e.g. based on a minimum size threshold for each identified object that is determined by the resolution of the images.

The algorithm performs two distinct analyses: A segmentation method optimized for identifying particles and a classification method optimized for classifying each pixel to assess the overall area coverage of different phases:

- The segmentation approach uses narrower grey-scale thresholds than the classification method and a relatively small Gaussian filter mask to increase edge-contrast and avoid counting several particles as one big agglomerate. It aims at deriving robust statistics regarding the number of particles and their size distribution. The narrower thresholds may lead to under-prediction of particle counts due to false-negative. Data from this approach is, however, ideal to observe relative changes in particle numbers and size distribution between samples.
- The classification approach uses wider grey scale intensity threshold ranges and a much larger Gaussian filter mask (blurring the whole image to "make similar things more similar") so that the general differentiation between different phases is improved at the expense of particle differentiation due to lower edge contrast. This method was applied to calculate the relative amounts between large particles and clusters of small particles as will be described in section 2.5.

To make the particle segmentation results statistically comparable, the same filter parameters (gaussian filter size, grey scale ranges, etc.) were applied to all images. The algorithm was manually tuned to give a qualitatively satisfying result for a random representative sample before analyzing the rest of the samples using the same parameters. Analysis of multiple samples allows to derive meaningful results despite the possible errors in individual images.

The area of each segmented particle was calculated from pixel counts by applying a conversion factor derived from the scale bar in each image. The resulting area was converted to equivalent diameter considering circular area, which was in turn used to calculate particle volumes considering spherical particles. Particle size specific volume fractions v_i were then calculated as $v_i = \frac{V_i}{V_{tot}}$, where V_i is the integrated volume of all the particles of size fraction i and V_{tot} is the integrated volume of all the particles within an image.

Twenty size fractions or "bins" logarithmically distributed between 0.1 and 300 μm are used to display particle size distributions and corresponding particle capture efficiency results.

2.4.2. Particle Diffraction Sizer (PDS)

An LA-960 Laser Particle Size analyzer with an ultrasonic probe was used to measure particle size distributions of the off-gas dust samples, HGS and rear deposits (A Guidebook to Particle Size Analysis, n.d.). Iso-propanol was utilized as dispersive media and ultra-sonication was applied in order to avoid particle agglomeration. For the case of HGS samples, manual milling with a mortar was performed before suspension in iso-propanol. Mie scattering theory was used to calculate particle size specific volume fractions v_i from light diffraction data.

2.5. Particle deposition analysis

The area-averaged deposit thickness $\bar{l}_d$ at the front and rear sides of the cold-finger were calculated by averaging the local deposit thickness of 22 equally spaced EPMA images over the half-circumference of the tube/deposits cross section. The corresponding time-and-area-averaged mass deposition flux is given by:

$$\bar{J} = \bar{l}_d \rho_d / t \tag{1}$$

where ρ_d is the estimated deposit thickness (see section 2.3) and t is the experiment duration.

The capture efficiency parameter η is defined as the fraction of the mass flux through the projected area of the substrate that is deposited (captured). It follows that the time-averaged capture efficiency can be expressed as $\bar{\eta} = \frac{\pi}{2} \frac{\bar{J}}{u_{bulk} C_p}$, where u_{bulk} is the bulk velocity of the off-gas and C_p is the particle mass concentration in the off-gas. Introducing the particle size-specific average mass deposition flux, $J_i = \bar{J}\, m_{i,d}$, and particle mass concentration, $C_{p,i} = C_p\, m_{i,off}$, where $m_{i,d}$ and $m_{i,off}$ are the mass-fractions of particle size i in the deposit and off-gas, respectively, the size-specific average particle capture efficiency is expressed as

$$\bar{\eta}_i = \frac{m_{i,d}}{m_{i,off}} \bar{\eta} \tag{2}$$

Size-specific particle volume fractions v_i, taken from the experimental particle size distributions obtained from EPMA IA measurements were directly used in place of mass-fractions $(m_{i,d},\ m_{i,off})$ since it was not possible to differentiate between mass-densities of individual particles.

2.5.1. Off-gas samples

Due to the large polydispersity within off-gas particles, each sample was analyzed using two different magnifications (40x and 1000x). In addition, particle size distribution of segregated regions in the off-gas images consisting of sub-micron particle clusters were analyzed independently (i.e. by analyzing random areas within the clusters) at a magnification of 2000x.

In order to combine the results from different magnifications, the following method was used. First, the integrated volume concentration of the different size fractions C_i was calculated for each magnification j as $C_i = \frac{V_i}{A_{im}}$, where V_i is the integrated volume of particles of size fraction i and A_{im} is the total image area. The values of C_i for the three different magnifications were then averaged and normalized in order to calculate a global size distribution of volume fractions v_i as follows:

$$v_i = \frac{\widehat{C}_i}{\sum_{i=1}^{ni} \widehat{C}_i}, \tag{3}$$

where $\widehat{C}_i$ is the weighted average concentration for the size fractions i overlapping in the different magnifications calculated as follows:

$$\widehat{C}_i = \frac{1}{N} \sum_{j=1}^{N} C_{i,j}\, w_j \tag{4}$$

With j iterating through the different magnifications used to characterize a given off-gas sample.

For the non-overlapping fractions (i.e. fractions that fall below or above detection limits of the images), only the fractions with values were used (no averaging with "empty" fractions).

The weight parameter w_j, was only used when computing the particle concentration within the particle clusters (2000x magnification) to transform them into particle concentrations relative to the whole image area (A_{im}). It was calculated as $w_j = \frac{A_{clust}}{A_{im}}$, where A_{clust} is the integrated area of the particle clusters within the 40x magnification images, measured using the classification method described earlier.

Particle capture efficiencies were plotted against Stokes number which is defined as the particle's response time divided by the fluid's response time and can be expressed as:

$$Stk = \frac{d_p^2 \rho_p u_{bulk}}{18 \mu_f D_{cyl}} \tag{5}$$

where d_p and ρ_p are the particle diameter and mass density, u_{bulk} and μ_f are the off-gas bulk velocity and dynamic viscosity, and D_{cyl} is the cold-finger diameter. The particle mass density was calculated as the weighted average between the main phases (alumina, cryolite, chiolite and atmolite) in the different samples measured by qualitative XRD in a previous study by the authors (Clos et al., 2019).

3. Results and discussion

3.1. Deposits growth rates and densities

In order to visualize the growth rates of the deposits, results for the maximum deposits thickness for front HGS and rear deposits,

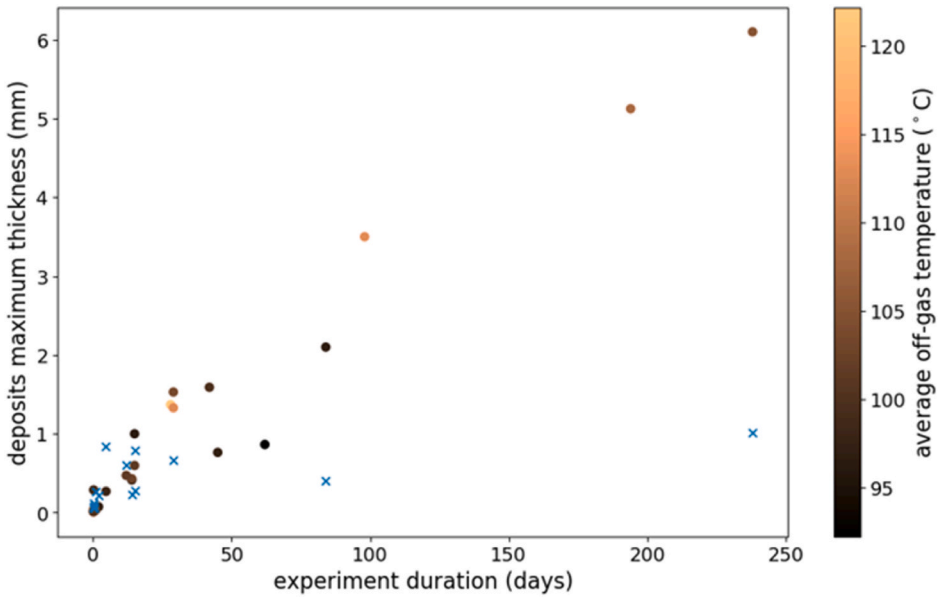

Fig. 2. Maximum deposits thickness at the front (circles) and rear (crosses) side stagnation points.

measured in the stagnation points as a function of the total experiment duration are displayed in Fig. 2. The maximum thickness is shown instead of the area-average thickness used in the capture efficiency studies (i.e. in equation (1)), as this value is more relevant for potential equipment clogging studies. The ratio between maximum and average thickness was not observed to have a time dependence and has an average value of 5.4 for front HGS and 2.5 for rear deposits across different experiments.

The values for the front HGS are displayed in a colormap as a function of the average off-gas temperature during the whole experiment. Variations in average off-gas temperatures are mainly a function of changes in weather conditions. Both off-gas and atmospheric temperatures were shown to have a positive correlation on HGS growth rates in secondary alumina transport pipes (Bock Haugland et al., 2019).

As can be seen from Fig. 2, the maximum thickness of HGS has a linear dependency over time, meaning that the growth rates do not stabilize. Moreover, it is also possible to appreciate a weak correlation between higher average off-gas temperatures and growth rates. A possible explanation for this effect is that higher levels of humidity in the off-gas at higher ambient temperatures, increase the adhesion properties of the particles, as was observed in other studies (Bateman et al., 2014; Wu et al., 1992).

It can also be seen from Fig. 2 that the rear deposits maximum thickness is achieved after approximately two weeks, which indicates a stabilization between deposition and re-entrainment. Unfortunately, many data points for the rear deposits thickness are missing as they were not considered at the initial stages of the study. The temperature for the rear deposits experiments has not been included in the colormap for clearer visualization of HGS results and considering that no such correlation was observed for these types of deposits. This is probably due to masking from particle re-entrainment effects.

The thickness of both front HGS and rear deposits for the few-hour experiments vary by an order of magnitude, which cannot be appreciated in the figure with linear Y-axis. This suggests large local variations in the off-gas dust load which can be related to pot cell operations.

The time evolution of front HGS deposits morphology can be seen in Fig. 3. Due to the larger deposition rates at the stagnation point, an advancing wedge-shaped deposits front is formed after approximately a month.

The average mass densities for front HGS and rear deposits have estimated values of 2246 and 457 kg/m^3, respectively, using the methods described in section 2.3. In rear deposits density estimation, it is assumed that the level of porosity of the particles in the glass containers is similar to the deposits, given the fact that no significant mechanical compression is applied in neither the deposited particles (no dynamic pressure on the wake) nor the containers where gravity is small compared to inter-particle forces.

3.1.1. *Iso-thermal growth rates*

Three isothermal experiments (i.e. in absence of coolant flow) were run for two weeks with results displayed in Table 1. The durations of the experiments were chosen considering the growth stabilization of the rear deposits after two weeks. No thermophoretic effects were observed in the growth of HGS in any of the three iso-thermal experiments. On the contrary, two of the experiments resulted in a drastic 90% reduction in the rear deposits growth rates. The third experiment however, resulted in a growth rate close to the average growth of the non-iso-thermal two-weeks experiments. However, the extremely low rear deposits growth rates for two of the iso-thermal experiments strongly indicate a relatively important thermophoretic effect. The deviation in the third result might be due to a period of increased dusting in the particle size range relevant for rear deposits formation. Rear deposits have a larger standard deviation (58%) in growth rates (with similar experiment duration) compared to front HGS (36%) samples.

3.2. *Determination of particle concentration and size distributions*

3.2.1. *Off-gas characterization*

In the present study, the off-gas flowing across the cold-finger is produced by over a hundred aluminium reduction pot cells. Off-gas dust concentrations in the duct where the experiments take place are measured every trimester. Results from the last four years show an average concentration of 2.7 g/m^3 with a 30% standard deviation. Pot cell operation has a great influence on the properties of the

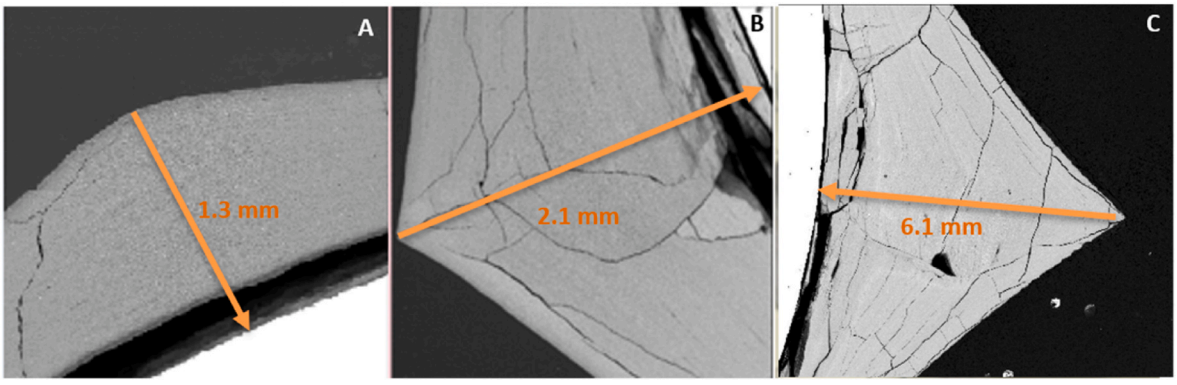

Fig. 3. BSE electron images of HGS/metal interface showing the wedge-shape evolution in experiments with increasing durations: A: 29 days: B: 84 days, C: 238 days. The arrows point in the off-gas flow direction.

Table 1
Results from the three 14-days duration, iso-thermal experiments.

Average temperature (°C)	Maximum thickness front HGS (μm)	Maximum thickness rear HGS (μm)
94	497	51
116	603	508
104	670	57

generated off-gas, which can explain the large variation in off-gas particle concentration. For example, fan suction power is increased when operations on individual cells are performed in order to reduce cell emissions to the pot room. Increased air suction will generally reduce the off-gas dust concentration whereas other events such as alumina feedings and anode effects, may increase dusting from individual cells by a factor of three (Gaertner, 2013). The different amount of fines between raw alumina batches supplied to the pot cells is also a factor that contributes to the variability in off-gas dust loads.

In the present study, different image magnifications (40x, 1000x and 2000x) were used to quantify the off-gas particle size distributions, given their large polydispersity.

An example of a low magnification (40x) BSE image of an off-gas dust sample and the corresponding IA result is shown in Fig. 4. Besides the distinguishable bright particles (yellow), a grey diffuse phase is also identified (red), which was observed to consist of submicron particle clusters. The classification method was used to calculate the relative area coverage of the particle clusters in the images, as described earlier.

Twenty intermediate magnification images (1000x) were analyzed for each sample in order to quantify the small particles falling below the low limit detection from the low magnification images. Two sets of images in this magnification level are displayed in Fig. 5. Particles larger than 10 μm were filtered out of the IA particle counting in order to reduce errors arising from partly protruding particles in the image. The large polydispersity present in off-gas dust particles results in 65% average variance within the different size fractions of different images from the same sample. When comparing different samples (each sample consisting of an average of twenty images) the same variance is reduced to only 15%, which is a good measure of the statistical robustness of the method.

Finally, five high magnification (2000x) images were taken from the diffuse phase areas colored in red in Fig. 4. This revealed a cohesive submicron particle cluster structure, as can be seen in Fig. 6. Such fine particles are produced by condensation of the pot cells bath vapors with large supersaturation levels (20 times above the saturation pressure) achieved when the saturated bath vapors (970 °C) are mixed with the dilution air (25 °C) (L'vov et al., 2005). Due to the small particle sizes in these images, a substantial number of particles remained unsegmented. For this reason, a correction factor f was multiplied in the RHS of equation (4) to account for the unsegmented particles based on area coverage when subtracting the background; $f = (A_{im} - A_{back})/A_{seg}$, where A_{im} is the total area of the image, A_{back} is the background area (black) and A_{seg} is the integrated area of the segmented particles (green).

The combined particle size distribution results in volume % from the different magnifications, averaged across various off-gas samples, are displayed in Fig. 7 together with the corresponding averaged results from PDS analysis of the same samples and PDS results from Fleer et al. (Fleer, 2010). The comparison between these two techniques is intended to be at a qualitative level since they intrinsically measure different particle size characteristics.

PDS results from both studies have a similar mode value around 20 μm. However, lower particle sizes were detected in the study by M. Fleer (Fleer, 2010), with 25% in volume of the particles below 10 μm size range, whereas in the present work this fraction only accounts for 10% of the total.

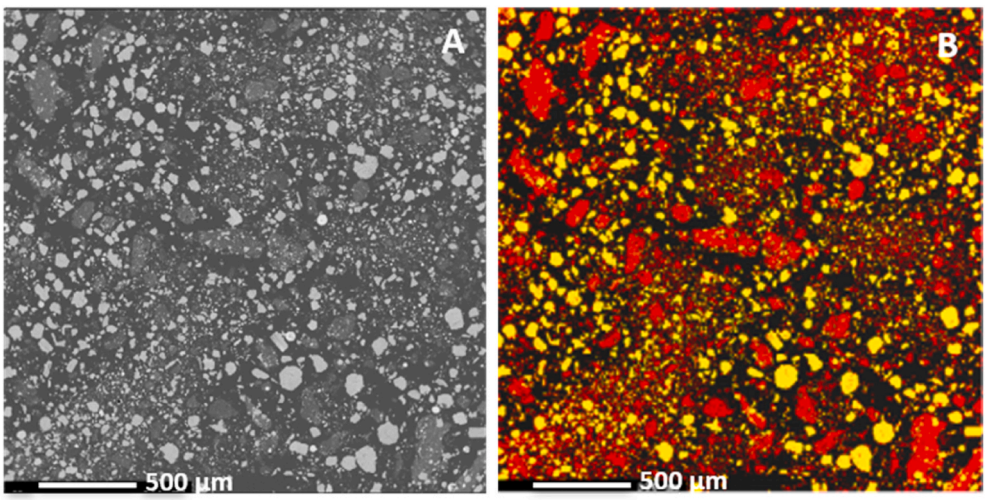

Fig. 4. BSE image of an off-gas sample (left) and corresponding classification IA (right) of large particles (yellow) and diffuse particle clusters (red). (For interpretation of the references to color in this figure legend, the reader is referred to the Web version of this article.)

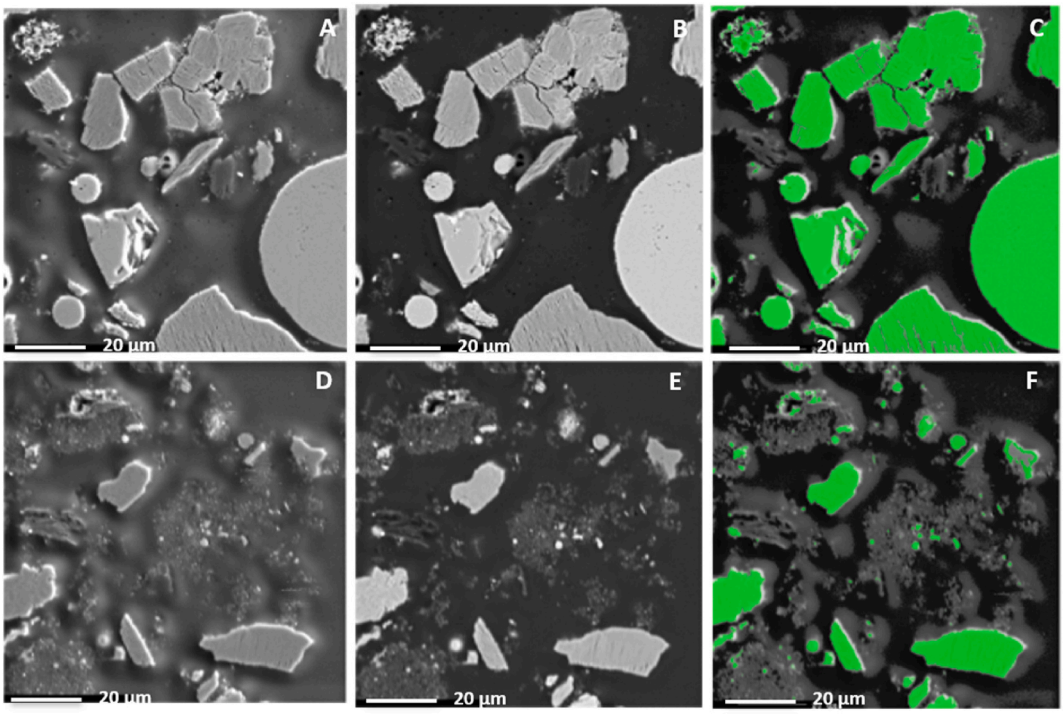

Fig. 5. SE images (left), BSE images (center) and segmentation IA images (right) of two samples (top, down) of off-gas particles at 1000x magnification.

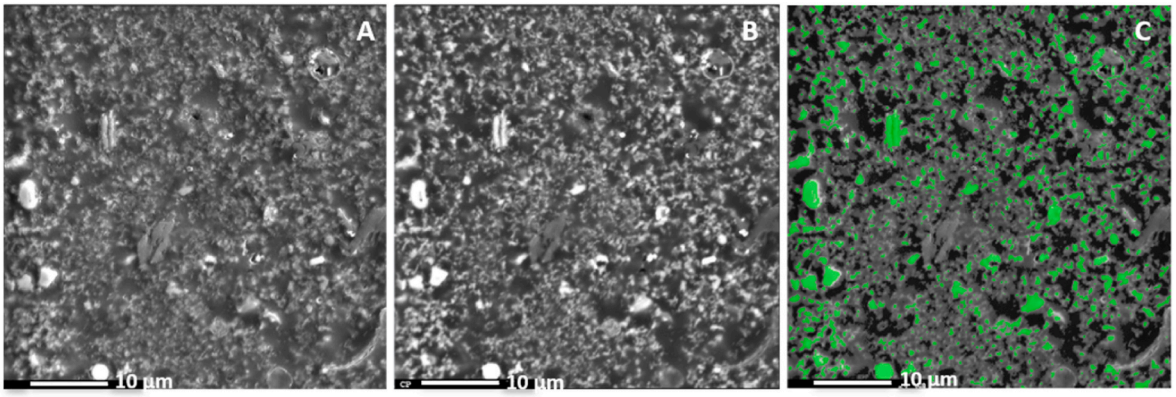

Fig. 6. SE (left), BSE (center) and segmentation IA (right) of a 2000x magnification image from an off-gas particle cluster.

The differences might be partially explained by the different dispersive media used in PDS measurements (this work: iso-propanol, Fleer (Fleer, 2010): water and air). M. Fleer (Fleer, 2010) compared both water and air cases and found a shift towards smaller sizes when using air, which indicated that air was able to better disperse the small particle fraction.

Image analysis results have a larger mode value of 50 µm and a larger fraction of small particles. Aggregation of small particles on the surface of larger particles in PDS analysis might contribute to the differences observed between the techniques, which is consistent with larger maximum particle sizes measured in the present PDS case.

The particle size distribution results from the IA of off-gas samples are calculated considering that the particles in the particle clusters shown in Fig. 6 are completely dispersed in the off-gas. This seems reasonable considering the low particle concentrations in the off-gas (6.3×10^{-7} m^3 particles/m^3 air).

The assumption of full dispersion of submicron particles in the off-gas duct is further evaluated by the in-situ particle size distribution analyses performed by Næss et al. (Næss et al., 2006) and Gaertner et al. (Gaertner et al., 2012), which avoid particle agglomeration upon collection on filters. Again, this comparison is of qualitative nature given the different type of particle size characteristics measured by this technique.

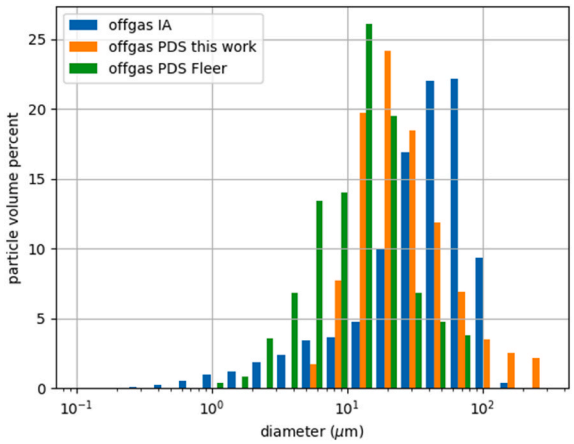

Fig. 7. Averaged particle size distribution in volume % from different off-gas samples analyzed by segmentation IA and PDS.

Næss et al. (Næss et al., 2006) used a cascade impactor to measure particle size distributions on isokinetically extracted off-gas from aluminium production cells. In their study 70% of the particles were smaller than 1 μm with a maximum particle size of 10 μm. The lack of larger particles might be due to lack of open cell operations and alumina feedings during off-gas sample extraction. This would result in lower fan suction rates and thus, reduced entrainment of larger particles.

Gaertner et al. used an Electrical Low-Pressure Impactor (ELPI) to measure the mass size distribution of off-gas particles with sizes below 10 μm from different aluminium plant smelters (see Fig. 8). Integration of the different size bins results in an approximate value of 130 mg/m^3 of particles with sizes below 10 μm. This result is 50% lower than the 270 mg/m^3 value obtained from combining image analysis (10% particles below 10 μm) and the average particle concentration in the off-gas (2.7 g/m^3) in the present study.

Given the large variability in off-gas dust loads, these results are consistent with the assumption that the sub-micron rich particle clusters observed in Fig. 6 are fully dispersed in the off-gas channel.

3.2.2. *Front HGS and rear deposits*

A morphology comparison between front HGS and rear deposits can be seen in Fig. 9 where SE and BSE images are displayed together with the corresponding particle-segmented picture from IA. Results for the rear deposits are quite satisfactory except for carbon particles which have a dark contrast similar to the epoxy resin. The concentration of this particles is low and should therefore not have a significant impact on the size distribution results.

The experiments-averaged particle size distribution results from IA analysis for front HGS and rear deposits are displayed in Fig. 10 together with the off-gas results. As can be seen from the figure, front HGS has a log-normal distribution centered around 1.2 μm with 35% of the particles in the submicron region. Such small particles are in the size range of the particle clusters shown in Fig. 6 originating from the quenching of the electrolyte bath vapors from the pot cells. Their small size allows them to fill the voids of the larger deposited particles resulting in a very compact structure that can explain the hardness and high surface adherence of this material.

The PDS analysis results from the HGS samples is not presented since stable measurements were not reached even with several hours of sonication. Measurements after sonication rounds resulted in a continuous shift towards smaller particle sizes with even the appearance of a submicron fraction at around 300 nm. It seems clear that the strong cohesive forces between the small HGS particles prevented them from being dispersed effectively with this technique.

PDS measurements for the rear deposits reach stable values after 1 min sonication and the results are in good agreement with those reported by M. Fleer (Fleer, 2010), who also analyzed such deposits in the rear side of a cylindrical cold-finger in an aluminium plant.

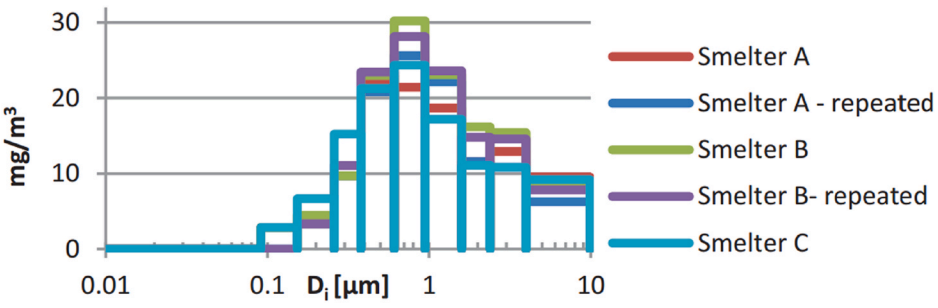

Fig. 8. Mass distribution from off-gas particles measured using an ELPI and particle density estimates from gravimetric analysis of collected size fractions. Reproduced with permission from Gartner et al. (Gaertner et al., 2012).

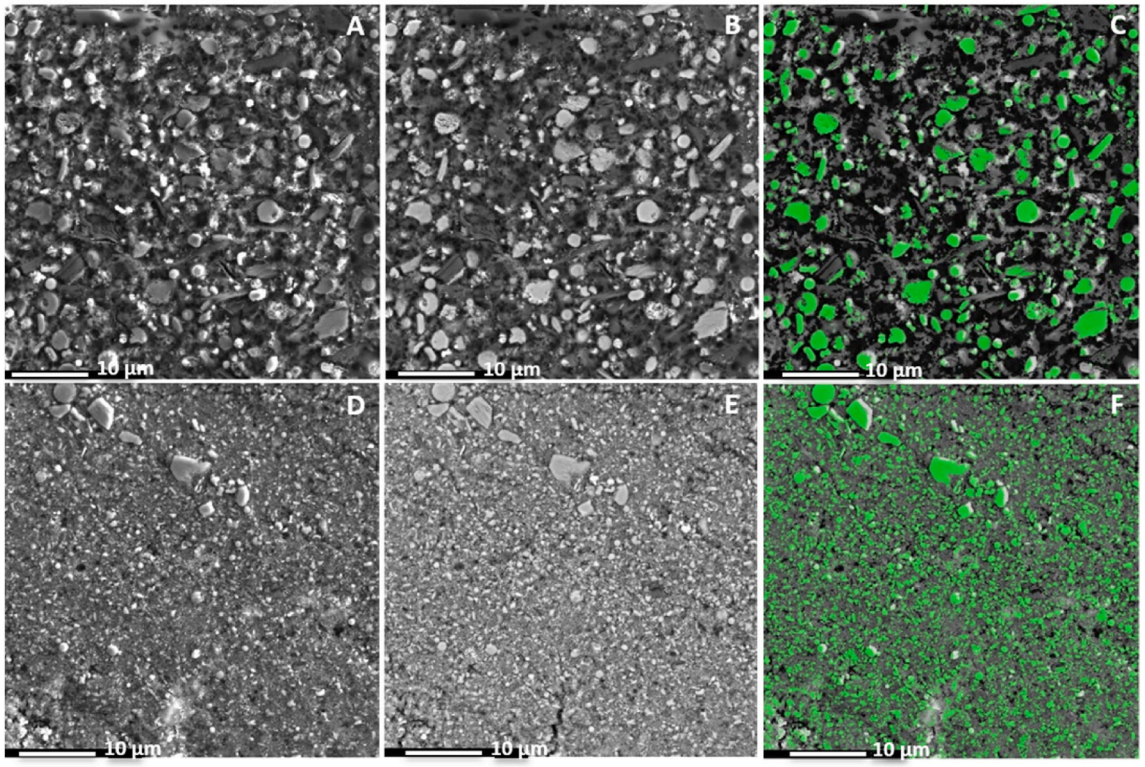

Fig. 9. SE electron images (left), BSE images (center) and IA segmented images (right) from a rear deposits (above) and a HGS sample (below).

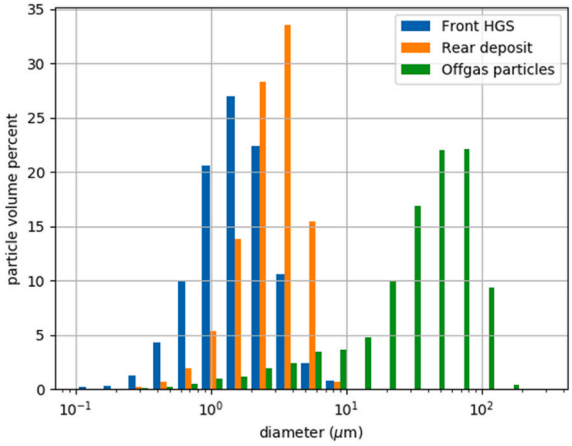

Fig. 10. Average particle size distributions for HGS, rear deposits and off-gas samples using IA.

Both PDS results are displayed in Fig. 11 together with the present results from IA. As can be seen from the figure, the three distributions have similar shapes although the values from PDS are shifted towards larger sizes. This might also be an effect of particle aggregation of the smaller particle fractions in the PDS analysis.

3.2.3. HGS from secondary alumina transport pipes

A different type of HGS is formed in the transport pipes of secondary alumina where the pipes bend 90° to take a turn. As discussed in the introduction, some key components absorbed from the off-gas must trigger the formation of HGS in these pipes since primary alumina transport pipes do not suffer from HGS formation.

In order to identify the common HGS forming agent, samples from the study by Haugland et al. (Bock Haugland et al., 2019) were collected and analyzed in the same manner as with the cold-finger samples. Fig. 12 displays electron images at low (A-C) and high (D-F)

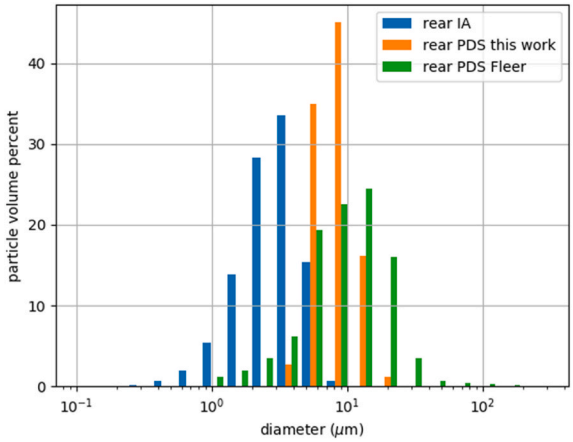

Fig. 11. Particle size distribution results from segmentation IA and from PDS from this work and Fleer et al. (Fleer, 2010).

magnification for primary (A and D) and secondary (B and E) alumina particles and the resulting HGS (C and F).

The morphology of the secondary alumina HGS grains has a wavy structure, opposed to the flat grains from cold-finger HGS, which is apparent to the naked eye and can also be seen in Fig. 12C. Fig. 12F is a zoom in of the area highlighted with the red square in image C. As can be seen from the figure, a sharp transition edge exists between an area with larger particles on the top and smaller particles on the bottom.

The main difference between primary and secondary alumina particles, besides the absorption of HF and other gaseous species from the off-gas, is the presence of the submicron particle clusters (highlighted by yellow squares in Fig. 12E) observed in the off-gas samples presented in section 3.2.1. These submicron particles are collected from the off-gas in the filters of the dry scrubber, and periodically

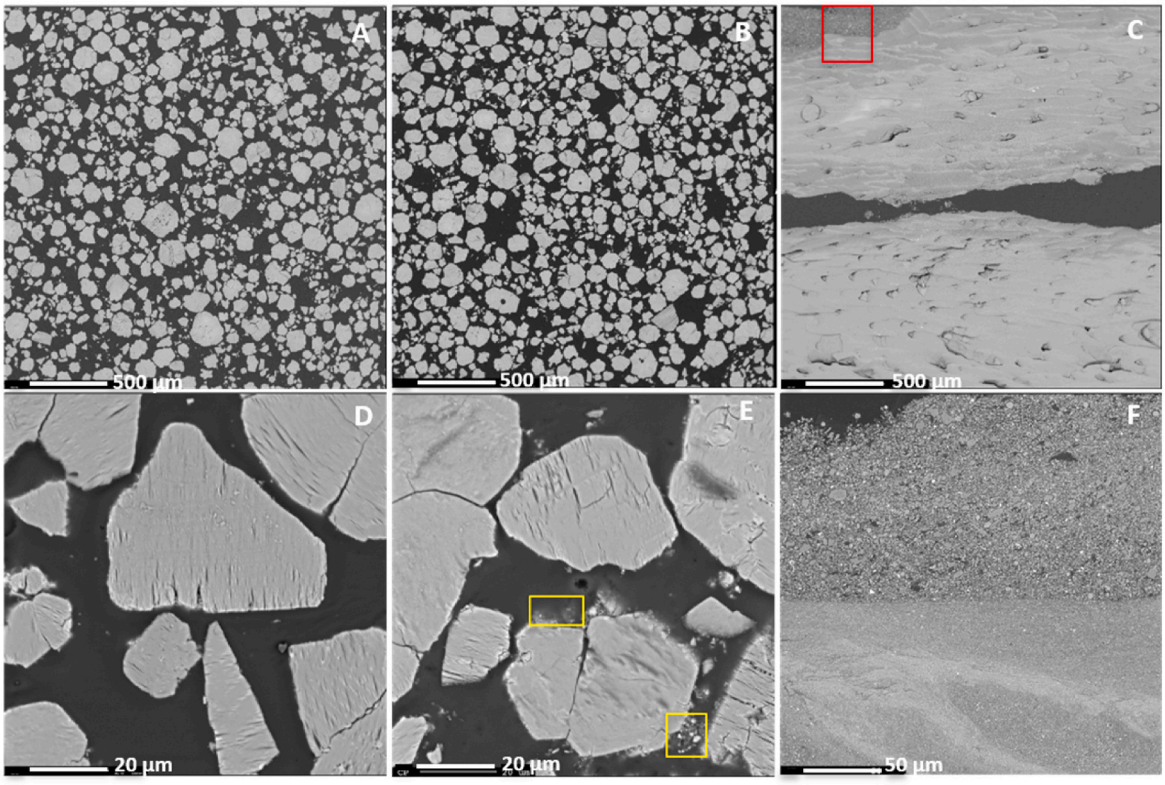

Fig. 12. BSE images from primary alumina particles at 40x magnification (A) and 1000x magnification (D), from secondary alumina particles at 40x magnification (B) and 1000x magnification (E) and from secondary alumina transport pipe HGS at 40x magnification (C) and 300x magnification (F) of the area enclosed by the red square in image (C). (For interpretation of the references to color in this figure legend, the reader is referred to the Web version of this article.)

shacken down and entrained in the secondary alumina stream at very low off-gas/alumina ratios.

The particle size distributions of both primary and secondary alumina are quite similar as can be seen in Fig. 13 where they are plotted together with the particle size distribution from the off-gas, for comparison. As can be seen in the figure, the off-gas larger particle sizes overlap with the smaller fractions of the secondary alumina particles, which are entrained by the air draft during alumina feedings to the pot cells.

In Fig. 14, SE and BSE images, as well as the corresponding IA-analyzed images from the two areas depicted in Fig. 12F, are presented. The corresponding particle size distribution is displayed in Fig. 15 together with the average results from the cold-finger HGS. The small particle size of the area with small particles in secondary alumina HGS required using a larger magnification (5000x) than with the HGS samples from the cold-finger (1000x).

As can be seen from Fig. 15, the particle size distribution of the cold-finger HGS falls between those from the secondary alumina HGS particles. The fraction of larger particles in the "big particles" HGS from secondary alumina is similar (in volume %) than that of the cold-finger rear deposits (see Fig. 10). However, the HGS has a much larger content of particles with sizes below 1 μm (20% for the HGS compared to 7% for the rear deposits), which is believed to be the key difference leading to the closely packed structure in the HGS sample.

Transmission electron microscope with energy dispersive spectrometry (TEM-EDS) measurements by Haugland et al. (Bock Haugland et al., 2019) showed that most of the particles in the secondary alumina HGS were alumina particles with sizes around 0.5 μm. It was also shown that *Na* was present in the intergranular region. It was argued that this sodium (*Na*) could be part of a binding phase formed by chemical reactions between NaF-AlF_3 or NaOH as a hydrolysis product.

It is, however, possible to appreciate a granular structure by zooming in on TEM-EDS image of the *Na* phase (Bock Haugland et al., 2019), which comprises particles in the size range of 50 nm. This in turn would be consistent with the presence of the smallest particles from the off-gas condensed atmolite ($NaAlF_4$) bath vapors, entrained in the dry scrubber, enhancing the adhesion properties of the depositing particles.

The fact that only alumina particles were observed in the HGS samples in Haugland et al. (Bock Haugland et al., 2019), as opposed to the mix between alumina and cryolite-like particles in the cold-finger HGS (Clos et al., 2019) indicates that the primary alumina stream already contains the building blocks of HGS in the size range of 0.5–5 μm but that it lacks the particle size ranges between 20 and 500 nm that are provided by the off-gas Atmolite condensed vapors, and which enable effective adhesion between the depositing alumina particles.

3.3. Deposition rates and capture efficiencies

As previously mentioned, the size-specific particle volume fractions presented in Fig. 10 were used as size-specific mass fractions m_i in order to calculate particle capture efficiencies using equation (2). Calculation of experiments-averaged growth rates for HGS and rear deposits yielded values of 31 and 809 μm/day, respectively. For the rear deposits with logarithmic growth rates over time, the initial deposition rates (i.e. t=0) should be used to omit particle re-entrainment effects. However, to avoid data extrapolation, a logarithmic function was fitted to the growth data (Fig. 2) and the value for 3 h deposition was used, which is the duration of the shortest experiment. The average off-gas velocity of 17 m/s, measured in the cold-finger duct (Clos et al., 2020, pp. 710–718), was used in the calculation of the capture efficiencies.

Results for the front and rear sides of the cold-finger are displayed in Fig. 16 and Fig. 17, respectively, together with other results from the literature. It is worth noticing that the different points in these graphs correspond with the particle size fractions presented in Fig. 10, i.e. the different Stokes values vary due to the different particle diameter of those size fractions. It is also worth mentioning that a value of 3600 kg/m^3 was used as average particle density in the calculation of the Stokes numbers, as described in section 2.5.1, which is different than the deposits density values used in the capture efficiency calculations (see Figs. 16 and 17).

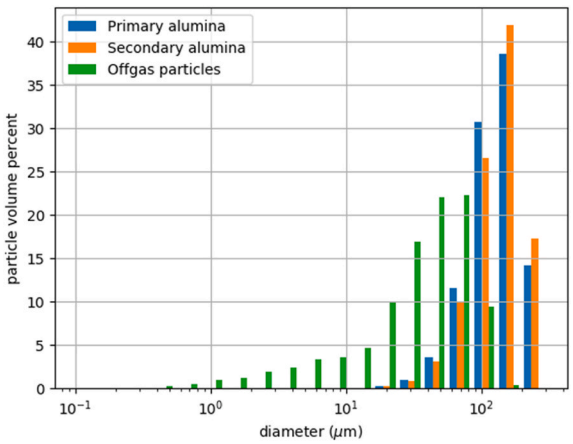

Fig. 13. Particle size distribution in volume % of primary and secondary alumina and off-gas particles.

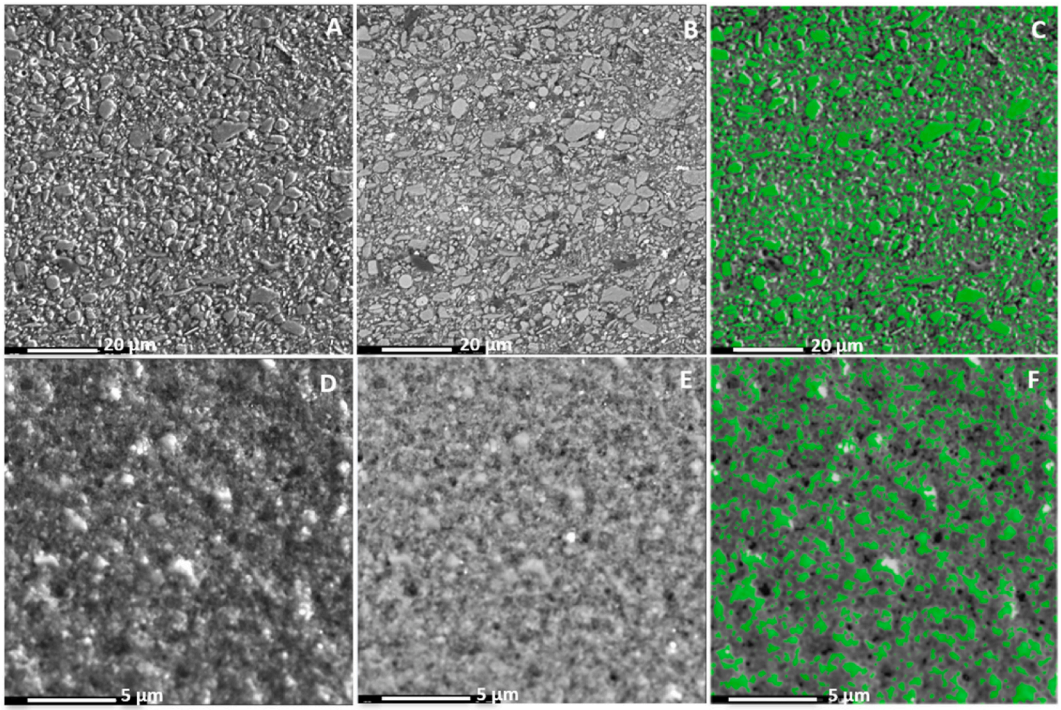

Fig. 14. SE images (left), BSE images (center) and segmentation IA images (right) of secondary alumina transport pipe HGS from the region with big particles (top) and the region with small particles (bottom) from Fig. 12F.

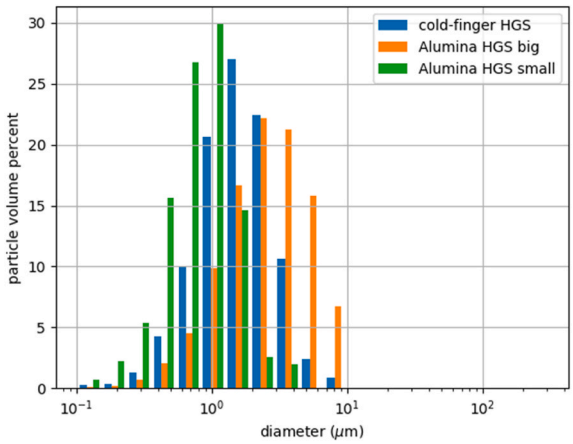

Fig. 15. Segmentation IA particle size distribution of HGS from cold-finger experiments and secondary alumina transport pipe for the area with big and small particles displayed in Fig. 14.

3.3.1. Front side

Kleinhans et al. (Kleinhans et al., 2019) employed Large Eddy Simulation (LES) and Haugen and Kragset (Haugen & Kragset, 2010) employed high order Direct Numerical Simulation (DNS) in Eulerian-Lagrangian modelling of fluid-particle mixtures to predict the impaction efficiency onto cylinders in cross-flow, as functions of Stokes number. As can be seen in Fig. 16 the present experimental capture efficiencies in the front side HGS are in the same order of magnitude than the numerical results for Stokes numbers <0.05. At higher Stokes numbers re-entrainment (Johnsen & Johansen, 2009) and rebounding (Wall et al., 1990) effects become important, and thus, the results deviate from the numerical models considering only impaction. The impaction mechanism for the particles in the region with low Stokes numbers (i.e. Stokes number <0.2) was described by Haugen and Kragset (Haugen & Kragset, 2010) as a "boundary interception model", where the particles virtually follow the fluid streamlines but impact the surface due to their finite radii.

Vincent and Humphries (Vincent & Humphries, 1978) performed wind tunnel particle deposition studies on the surface of a disc in

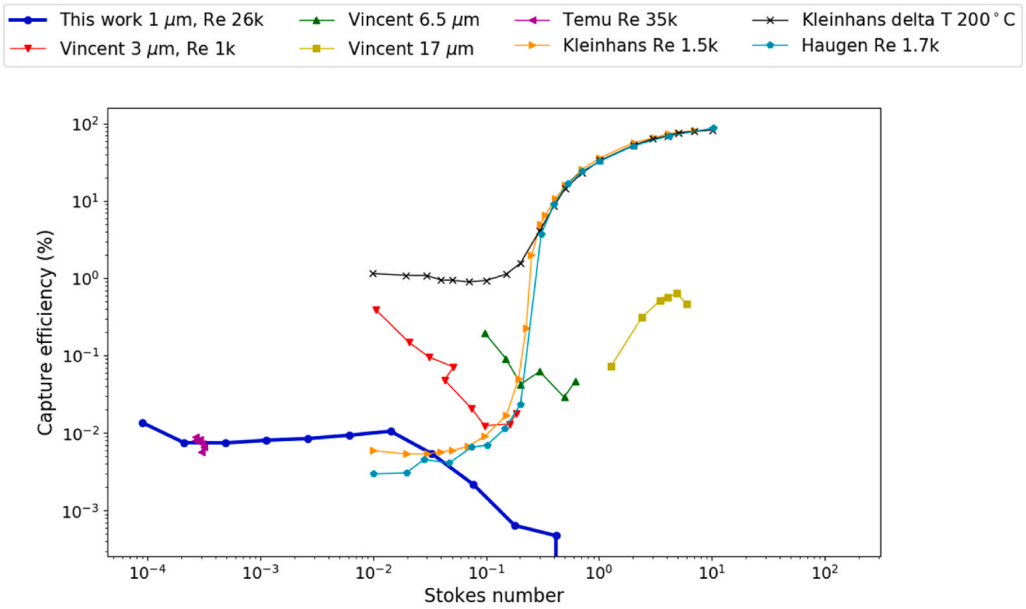

Fig. 16. Particle capture efficiency as function of the stokes number for different front deposits experiments from the present work and literature studies. Studies specifications include average particle sizes in the deposits (in μm), Reynolds number relative to the cylinder diameter (Re) and temperature difference between fluid and deposition wall (delta T). Kleinhans et al. (Kleinhans et al., 2019) and Haugen and Kragset (Haugen & Kragset, 2010) cases are numerical studies calculating particle *impaction* efficiency.

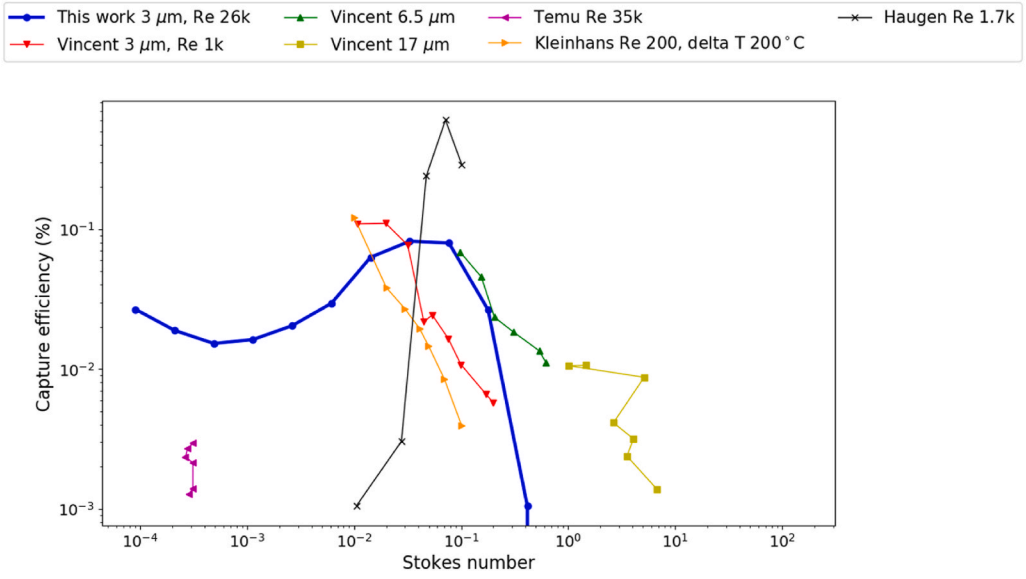

Fig. 17. Particle capture efficiency as function of the stokes number for different rear deposits experiments from present case and literature studies. Studies specifications include particle average sizes (in μm), Reynolds number (Re) and temperature difference between fluid and deposition wall (delta T). Kleinhans et al. (Kleinhans et al., 2019) and Haugen and Kragset (Haugen & Kragset, 2010) cases are numerical studies calculating particle *impaction* efficiency.

crossflow with commercial alumina particles of various particle size distributions. They found a minimum in particle capture efficiencies at a Stokes number around 0.1. For increasing particle sizes, the minimum shifted towards higher Stokes numbers. The increase in particle deposition at decreasing particle sizes in the low Stokes number region deviated from the inertial theoretical models discussed above. They argued that the increased deposition at lower Stokes numbers could be due to electrostatic charging of the particles, which were not included in the models. Such increase in capture efficiencies at lower Stokes numbers can also be seen in the present results, but as discussed above, this is consistent with rebound and re-entrainment effects.

The main deviation, however, is the lack of deposition of larger particles in the present study (Stokes numbers >0.3), whereas a deposition increase with Stokes numbers was observed by Vincent and Humphries (Vincent & Humphries, 1978). This difference might be due to the lower Reynolds number (1 order of magnitude) used in their study, as the larger inertia of the particles in the present study would result in higher re-bounding effects. Another factor could be the presence of rather large particles (100 μm) in the off-gas colliding with and thereby removing the less-attached, more-protruding big particles that might have deposited.

Temu et al. (Temu et al., 2002), who investigated the deposition of industrial Fe-Si particles onto a cylindrical probe in wind tunnel experiments, reported capture efficiencies similar to the values obtained in the present study. They did not provide with a detailed description of the particle size distributions, but they mentioned that 50% of the particles were below 1 μm.

Thermophoresis can have a big impact on the deposition of small particle sizes as predicted by Kleinhans et al. (Kleinhans et al., 2019) (see Fig. 16). Introducing a temperature difference of 200 °C between the fluid and the wall, increased the impaction efficiency of low Stokes region by almost three orders of magnitude. In the present study, however, no significant thermophoretic effects in average growth rates of HGS were observed between the iso-thermal experiments and the experiments with coolant flow. This might be due to the temperature differences between the off-gas and the surface of the cold-finger (≈10 °C) being too low to have a significant impact.

Brownian diffusion was not considered in neither of the simulations displayed here, which could potentially be relevant considering the small size of HGS particles. However, HGS formation occurs only in areas where the off-gas impacts a surface, which is a requisite for inertial deposition but not for Brownian diffusion. This observation together with the order of magnitude agreement with the inertial impaction simulation gives strong indication of a predominant inertial deposition mechanism in the formation of HGS.

3.3.2. Rear side

As can be seen in Fig. 17, a maximum in particle capture efficiency on the rear side in the present study is measured at a Stokes number of about 0.05. Haugen and Kragset (Haugen & Kragset, 2010) also obtained a maximum in particle impaction at the same Stokes number region. They discussed that particle deposition occurred due to the vortices formed in the rear-side wake which could accelerate particles with the right sizes towards the wall. They showed that increased Reynolds numbers resulted in larger impaction efficiencies with a shift towards smaller particles. They also argued that this was due to the formation of smaller vortices, with larger magnitude, and closer to the cylinder wall at larger Reynolds numbers.

The results from Kleinhans et al. (Kleinhans et al., 2019) on the rear side were calculated at a low Reynolds number of 200 where vorticity had no contribution on particle deposition which, was only caused by the thermophoretic force (200 °C). Significant thermophoretic effects were measured in two of the three isothermal experiments performed in this work, with a drastic reduction (90%) on the rear deposits average growth rates. The reason why thermophoretic effects have been observed in the formation of rear deposits as opposed to HGS growth might be explained by the longer residence time and lower inertia of the particles captured by the vortices in the wake which would increase the relative impact of the thermophoretic force compared to the front side.

Similar capture efficiencies were measured by the experimental deposition by Vincent et al. (Vincent & Humphries, 1978), although no decrease in capture efficiencies was observed at low Stokes numbers. Results by Temu et al. (Temu et al., 2002) are an order of magnitude lower which might be due to re-entrainment effects given the logarithmic growth nature of this kind of deposits.

4. Summary and conclusions

HGS formation in aluminium production off-gas systems has been investigated by conducting industrial HGS-gathering experiments in a cold-finger with durations ranging from 3 hours to 8 months. The obtained results clearly show that HGS growth has a linear dependency over time with no signs of growth stabilization. HGS formed at the front-side of the cold-finger with maximum growth rates in the stagnation point where the off-gas impinged the cold-finger, which diminished towards the probe sides forming an advancing wedge-shaped deposits front. HGS in the cold-finger experiments has an average growth rate of 31 μm/day with 36% standard deviation. On the rear side of the cold-finger dusty and loosely attached deposits were formed, which reached stable thicknesses after two weeks.

Particle size distribution of the deposits and off-gas dust samples, measured by IA and PDS techniques, are in good agreement. Front HGS has a log-normal size distribution centered at 1.2 μm with 35 volume-% of the particles in the submicron region. Rear deposits have a log-normal distribution centered at 3 μm with only 7 volume-% of the particles in the submicron region. It is suggested that the significant difference in deposit morphology between the front and rear side deposits is due to the larger submicron particles fraction in HGS generating a more closely packed structure.

An HGS sample from a secondary alumina transport pipe was analyzed and compared to the cold-finger HGS. Smaller particle sizes than those obtained in the cold-finger HGS were found with a log-normal distribution centered at 1 μm and with 75% of the particles below 1 μm. Entrainment and deposition of atmolite nano-particles in the range of 10–50 nm during the dry-scrubbing process is suggested to be the key ingredient in the formation of this type of HGS, acting as a binder between larger depositing particles and enabling a closely packed structure analogous to the HGS formed in the cold-finger.

Particle size distributions results obtained by IA were used to calculate particle capture efficiencies at the front and rear sides of the cold-finger as a function of Stokes number.

Particle capture efficiency results for HGS at low Stokes numbers agree well with numerical studies considering impaction efficiencies. At larger Stokes numbers (i.e. particle sizes) re-bound and re-entrainment effects result in lower capture efficiencies than those predicted by the simulated impaction efficiencies.

Capture efficiencies on the front side also compare well with similar experimental studies from the literature in the low Stokes

region, but deviate at large Stokes numbers, which is argued to be due to larger re-entrainment effects in the present study due to larger Re numbers and particle polydispersity.

A maximum particle capture efficiency at a Stokes number of 0.05 is found for the rear deposits, which is in good agreement with vorticity-induced particle deposition simulation results from the literature.

The overall results of the present study give an important insight on the particulate fouling nature of HGS and suggest that inertial deposition of small particles resulting in a closely packed structure is the main mechanism in the formation of HGS. Such knowledge might be useful in predicting how future changes in pot cell operation will affect the formation of HGS.

Preheating of the air sent to the pot cells to generate the off-gas could be used as an HGS formation mitigation strategy in order to reduce the quenching effect and thus increase the particle size of the condensed electrolytic bath vapors. However, this strategy would need to be linked with an active and efficient cooling system for the off-gas before reaching the GTC. At the same time, this strategy would also enable a more efficient recycling of the heat given the increased off-gas temperatures compared to the current conditions.

Declaration of competing interest

The authors declare that they have no known competing financial interests or personal relationships that could have appeared to influence the work reported in this paper.

Acknowledgment

The present work has been funded by the SFI Metal Production, (Center for Research-based Innovation, 237738), and the authors gratefully acknowledge the financial support from the Research Council of Norway and the partners of the SFI Metal Production. The authors also gratefully acknowledge the contributions of Birgitte Karlsen and Morten Peder Raanes in the preparation and analysis of EPMA samples.

References

Bateman, A. P., Belassein, H., & Martin, S. T. (2014). Impactor apparatus for the study of particle rebound: Relative humidity and capillary forces. *Aerosol Science and Technology, 48*(1), 42–52. https://doi.org/10.1080/02786826.2013.853866

Bock Haugland, I., Kjos, O., Røyset, A., Vullum, P. E., Aarhaug, A., & Halstensen, M. (2019). Alumina scale composition and growth rate in distribution pipes. *Light Metals*, 697–705.

Boerlage, S. F. E. (2001). *Scaling and particulate fouling in membrane filtration systems*. Taylor & Francis.

Bott, T. R. (1995). *Fouling of heat exchangers*. Elsevier Science B.V.

Clos, D. P., Johnsen, S. G., Nekså, P., & Aune, R. E. (2020). *The effect of hard scale deposition on the wall heat flux of a cold finger*. Light Metals.

Clos, D. P., Nekså, P., Johnsen, S. G., & Aune, R. E. (2019). Investigation on scale formation in aluminium industry by means of a cold-finger. *Light Metals*, 707–719.

Dando, N. R., & Lindsay, S. J. (2008). Hard grey scale. *Light Metals*, 227–232.

Fleer, M. (2010). *Heat recovery from the exhaust gas of aluminum reduction cells*.

Gaertner, H. (2013). *Characteristics of particulate emissions from aluminium electrolysis cells*. Norwegian University of Science and Technology (NTNU).

Gaertner, H., Ratvik, A. P., & Aarhaug, T. A. (2012). Impurity elements in raw gas ultra-fines from aluminium electrolysis cells. *Light Metals*, 839–844.

Gaertner, H., Ratvik, A. P., & Aarhaug, T. A. (2014). Raw gas particles and depositions in fume treatment facilities in aluminium smelting. *Light Metals*, 547–552. https://doi.org/10.1002/9781118888438.ch93

A Guidebook to Particle Size Analysis. (n.d.). Horiba Scientific. https://www.horiba.com/fileadmin/uploads/Scientific/Documents/PSA/PSA_Guidebook.pdf.

Haugen, N. E. L., & Kragset, S. (2010). Particle impaction on a cylinder in a crossflow as function of Stokes and Reynolds numbers. *Journal of Fluid Mechanics, 661*, 239–261. https://doi.org/10.1017/S0022112010002946

Johnsen, S. G., & Johansen, S. T. (2009). Development of a boundary condition wall function for particulate fouling CFD modeling. In *Seventh International Conference on CFD in the Minerals and Process Industries* (pp. 1–6). https://doi.org/10.13140/2.1.4561.4089

Kleinhans, U., Wieland, C., Babat, S., & Spliethoff, H. (2019). Large Eddy Simulation of a particle-laden flow around a cylinder: Importance of thermal boundary layer effects for slagging and fouling. *Fuel, 241*, 585–606. https://doi.org/10.1016/j.fuel.2018.12.056

Lindsay, S., & Dando, N. (2009). Dry scrubbing for modern pre-bake cells. *Light Metals*, 275–280.

L'vov, B. V., Polzik, L. K., Weinbruch, S., Ellingsen, D. G., & Thomassen, Y. (2005). Theoretical aspects of Fluoride air contaminant formation in aluminium smelter potrooms. *Journal of Environmental Monitoring, 7*(5), 425–430. https://doi.org/10.1039/b501302j

Næss, E., Slungaard, T., Moxnes, B., & Sonju, O. K. (2006). Experimental investigation of particulate fouling in waste heat recovery from the aluminium industry. *Fouling. Annals of the Assembly for International Heat Transfer Conference, 13*. https://doi.org/10.1615/IHTC13.p19.20

Temu, A. K., Næss, E., & Sønju, O. K. (2002). Development and testing of a probe to monitor gas-side fouling in cross flow. *Heat Transfer Engineering, 23*(3), 50–59. https://doi.org/10.1080/014576302753605376

Vincent, J. H., & Humphries, W. (1978). The collection of airborne dusts by bluff bodies. *Chemical Engineering Science, 33*(8), 1147–1155. https://doi.org/10.1016/0009-2509(78)85021-0

Wall, S., John, W., Wang, H.-C., & Goren, S. L. (1990). Measurements of kinetic energy loss for particles impacting surfaces. *Aerosol Science and Technology, 12*(4), 926–946. https://doi.org/10.1080/02786829008959404

Wu, Y.-L., Davidson, C. I., & Russell, A. G. (1992). Controlled wind tunnel experiments for particle bounceoff and resuspension. *Aerosol Science and Technology, 17*(4), 245–262. https://doi.org/10.1080/02786829208959574

Zedel, H., Fritzsch, R., Akhtar, S., & Aune, R. (2019). Estimation of aluminum melt filtration efficiency using automated image acquisition and processing. *Light Metals*, 1113–1120. https://doi.org/10.1007/978-3-030-05864-7_136